Measurement 256 (2025) 118388

Contents lists available at ScienceDirect

Measurement

journal homepage: www.elsevier.com/locate/measurement

WGINS: A wrist-worn GNSS/INS integrated system considering GNSS body shadowing

Xiaoji Niu [a,c], Zhihao Liu [a,b], Jian Kuang [a,c,*], Longyang Ding [a,b]

[a] GNSS Research Center, Wuhan University, Wuhan, China
[b] School of Geodesy and Geomatics, Wuhan University, Wuhan, China
[c] Hubei Technology Innovation Center for Spatiotemporal Information and Positioning Navigation, Wuhan, China

ARTICLE INFO

Keywords:
Pedestrian positioning
GNSS/INS integration
GNSS body shadowing
Wrist-worn PDR
Tightly-couple

ABSTRACT

Wrist-worn devices such as smartwatches have become increasingly popular consumer electronics in recent years. For smartwatches, positioning is considered a fundamental feature, and global navigation satellite system (GNSS) positioning is the primary solution employed for this purpose. However, GNSS positioning performance is inevitably affected by signal occlusion. In addition to traditional obstructions such as high-rise buildings, the human body itself could be a new occlusion source for the embedded GNSS antenna, and this phenomenon is termed GNSS body shadowing. This paper first illustrates and analyzes the impacts of GNSS body shadowing on GNSS pseudorange observations. Then, a wrist-worn and tightly-coupled GNSS/inertial navigation system (INS) integrated system (i.e., WGINS) is proposed, which takes GNSS body shadowing into account. Several tests have been conducted in an open-sky environment with the GNSS antenna worn on the wrist. Test results show that significant ranging errors in pseudorange observations can be determined when the satellites are shadowed by human body. The proposed WGINS utilizes high-frequency position and attitude information output from INS-based pedestrian dead reckoning (PDR) to identify obstructed satellites, which effectively mitigates the impacts of GNSS body shadowing on positioning performance. Test results demonstrate that the proposed WGINS reduces the horizontal position error from 2.42 m (root-mean-square, RMS) to 1.71 m.

1. Introduction

The emergence of pedestrian positioning technology has significantly enhanced the convenience of daily life. With the rapid development of wearable technologies, wearable devices have become an ideal option when considering location-based services (LBS) [1]. Among various products, wrist-worn devices such as smartwatches and wristbands have become increasingly popular consumer electronics in recent years. For smartwatches, major manufacturers now consider positioning as a core function [2], enabling applications such as outdoor sports tracking, map navigation, child or elderly safety, etc. Consequently, there is a clear demand for wrist-worn devices to provide continuous and reliable location services in different application scenarios.

For smart devices, the embedded global navigation satellite system (GNSS) chips are typically employed to provide the user's location. As a basic method, various positioning methods have been developed. For the basis, standard point positioning (SPP) can provide a meter-level positioning accuracy [3]. By using reference station, such as differential GNSS (DGNSS) [4] and real-time kinematic positioning (RTK) [5], the positioning accuracy can be further improved. While in urban canyons, the positioning performance is mainly affected by multipath effects and non-line-of-sight (NLOS) receptions, and the relative positioning methods are not so efficient in this case; thus, three-dimensional city model [6] and pedestrian map [7] are used to mitigate the impacts of signal blockage and reflection. It should be noted that these investigations are conducted using smartphones, but the mentioned solutions can be adopted in wrist-worn devices to some extent. Nevertheless, an important issue overlooked in previous studies is that the GNSS signal could be obstructed by human body in wrist-worn scenarios. Researchers have verified that human body is a significant propagation impairment for wireless systems operating in indoor environments [8], and a shadow region (i.e., body shadowing) will be generated when mobile devices proximate to human body [9]. Similarly, human body could naturally become a new occlusion source when GNSS antenna is mounted on the user's wrist, and this phenomenon is termed as GNSS body shadowing in this paper.

* Corresponding author at: GNSS Research Center, Wuhan University, Wuhan, Hubei Province, China 430072.
E-mail address: kuang@whu.edu.cn (J. Kuang).

https://doi.org/10.1016/j.measurement.2025.118388
Received 5 April 2025; Received in revised form 4 July 2025; Accepted 8 July 2025
Available online 18 July 2025

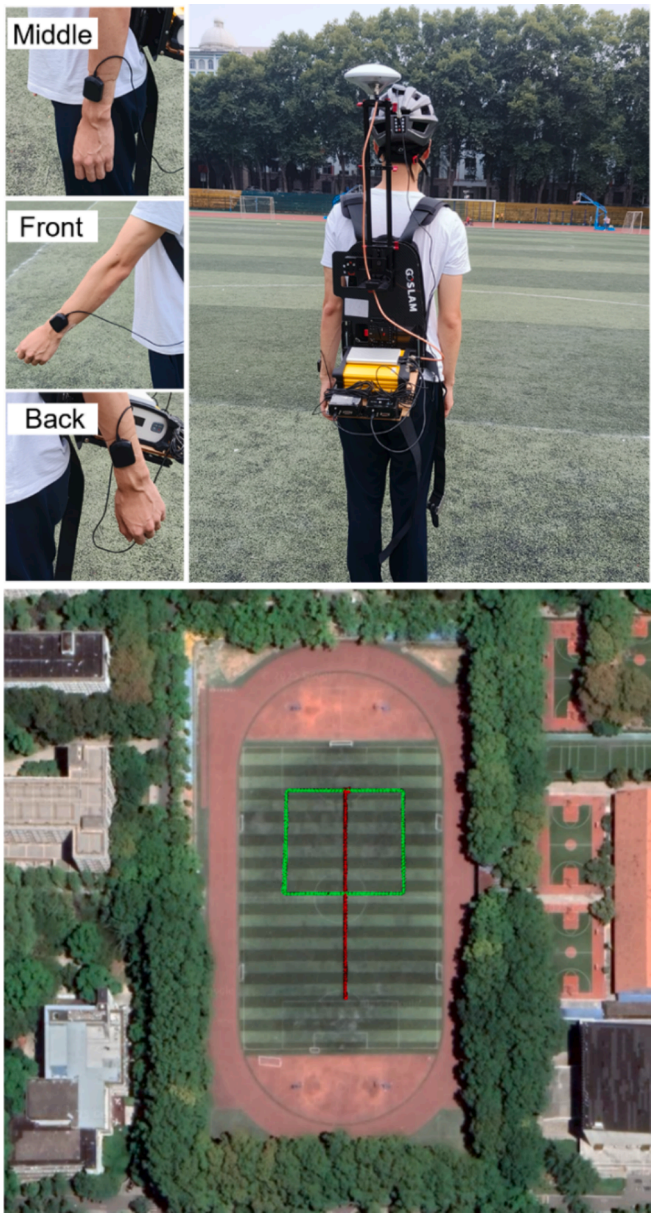

Fig. 1. Experimental setup (top panel) and kinematic test trajectories (bottom panel).

Additionally, in environments where GNSS signals are degraded or unavailable, inertial measurement unit (IMU) has been widely used for pedestrian positioning through a technique known as pedestrian dead reckoning (PDR) [10]. In 2011, wrist-worn accelerometer and GPS was first employed to estimate step length [11]. Then, [12] proposed a complete wrist-worn PDR system, which takes motion recognition into account. Subsequently, a special wrist-worn PDR system has been designed for those who use a front-wheeled walker [13]. Furthermore, researchers deeply analyzed the suitability of wrist-worn sensors for implementing PDR systems, and the authors are optimistic about the feasibility [1]. Other studies have focused on specific components of wrist-worn PDR, such as step detection [14], walking speed estimation [15], and step length estimation [16]. It can be found that only a few wrist-worn PDR algorithms have been proposed, and the unique characteristics of wrist-worn scenarios have not been fully considered.

In outdoor environments, it has been demonstrated that combining GNSS with IMU-based PDR can effectively improve the positioning accuracy in smartphone-based pedestrian navigation [17]. However, only limited research has explored this approach for wrist-worn devices. There are two key differences between wrist-worn devices and smartphones that require special attention. On the one hand, since wrist-worn devices are worn in close contact with human body, the impacts of GNSS body shadowing should be considered, which has not been noticed in previous studies. On the other hand, the motion characteristics of wrist-worn devices differ from those of smartphones. In most cases, the wrist-worn device swings with the arm while the smartphone is held in the hand, which requires special consideration in the design of PDR algorithms.

In view of the above-mentioned issues, a wrist-worn GNSS/INS integrated system (i.e., WGINS) for pedestrian positioning is proposed, which takes GNSS body shadowing into account. In this paper, the impacts of GNSS body shadowing on pseudorange observations are illustrated and analyzed. Then, a strapdown INS-based PDR is specifically designed for wrist-worn sensors. Thereafter, according to the position and attitude information provided by PDR, the obstructed satellites can be detected. Finally, the detected satellites are down-weighted with corresponding weighting strategies, and the impacts of GNSS body shadowing can be mitigated. The contributions of our work can be summarized as follows:

(1) According to the tests conducted in an open-sky environment, the impacts of GNSS body shadowing on pseudorange observations have been investigated quantitatively for wrist-worn devices.
(2) Aiming at wrist-worn scenarios, a specifically designed INS-based PDR algorithm is proposed, which combines with GNSS in a tightly-coupled mode and helps to mitigate the impacts of GNSS body shadowing.

The remainder of this paper is organized as follows. First, the impacts of GNSS body shadowing are illustrated and analyzed. Then, the proposed wrist-worn GNSS/INS integrated system is described in detail. Subsequently, the test results and analysis are presented. Finally, conclusions and future works are summarized.

2. Illustration of GNSS body shadowing

To illustrate GNSS body shadowing, GNSS observations are collected in an open-sky environment. The effects are then described and analyzed through both static and kinematic tests. Finally, the shadow region has been determined, providing a basis for subsequent algorithm design.

2.1. Experimental description

All tests were conducted on a playground using a single-frequency GNSS antenna mounted on the participant's left wrist (the top panel of Fig. 1). For comparison, an additional GNSS antenna was mounted on the helmet to ensure there is no signal occlusion. Additionally, a geodetic GNSS receiver and two INS-Probes (an integrated navigation module consisting of u-blox F9P and TDK ICM-20602) were employed for data collection.

In this section, both static and kinematic tests were conducted. In the static test, the participant remained stationary while holding the left wrist in three different positions: middle, front, and back, as illustrated in the top panel of Fig. 1. Each position was maintained for 10 min, and 30 min of data collection was counted as one complete test. In the kinematic test, the participant walked along straight and square routes, with natural arm swing. In this case, 10 min of GNSS data were collected for each route.

2.2. Impacts analysis of GNSS body shadowing

For consumer applications, pseudorange is the most basic measurement in GNSS positioning algorithms. Therefore, the impacts of GNSS body shadowing on pseudorange observations are primarily focused on

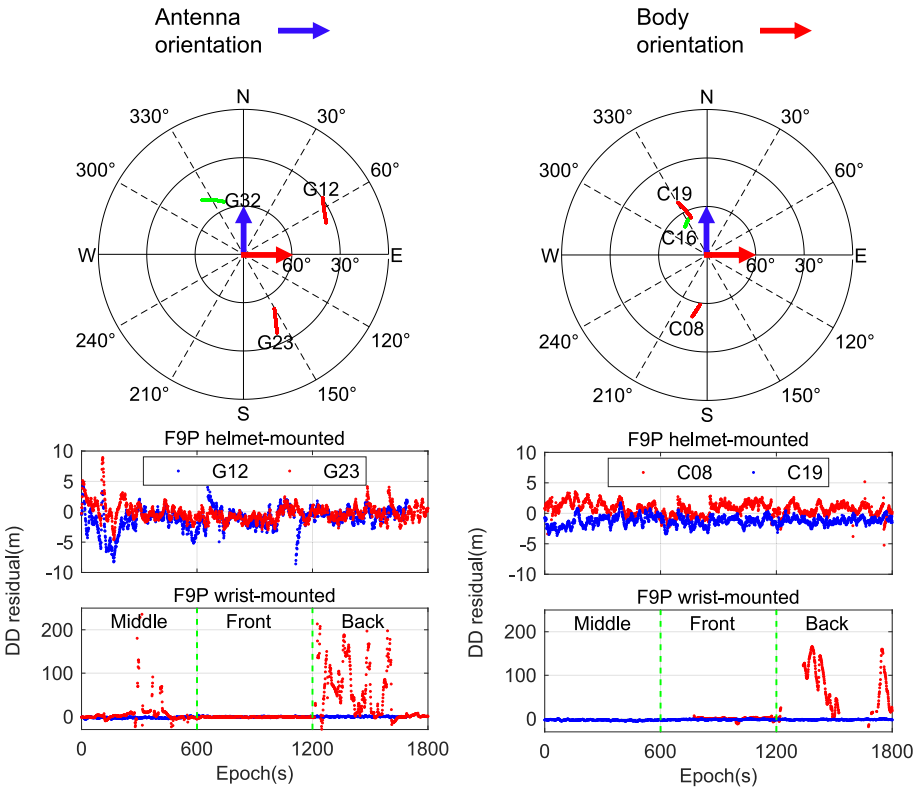

Fig. 2. Sky plot and DD residuals in helmet-mounted and wrist-mounted scenarios for GPS and BDS. Use satellites G12, G23, C08, and C19 as example; satellites G32 and C16 are selected as reference satellites.

in this paper. When the satellites are obstructed by the human body, ranging errors in pseudorange observations can be observed. To detect ranging errors from raw measurements, the double-differencing technique is adopted, as most errors such as satellite and receiver clock-biases, atmospheric effects, and multipath effects can be eliminated [18]. The double-differenced (DD) pseudorange observation can be expressed as:

$$P_{rb}^{ij} = \rho_{rb}^{ij} + \varepsilon_P \tag{1}$$

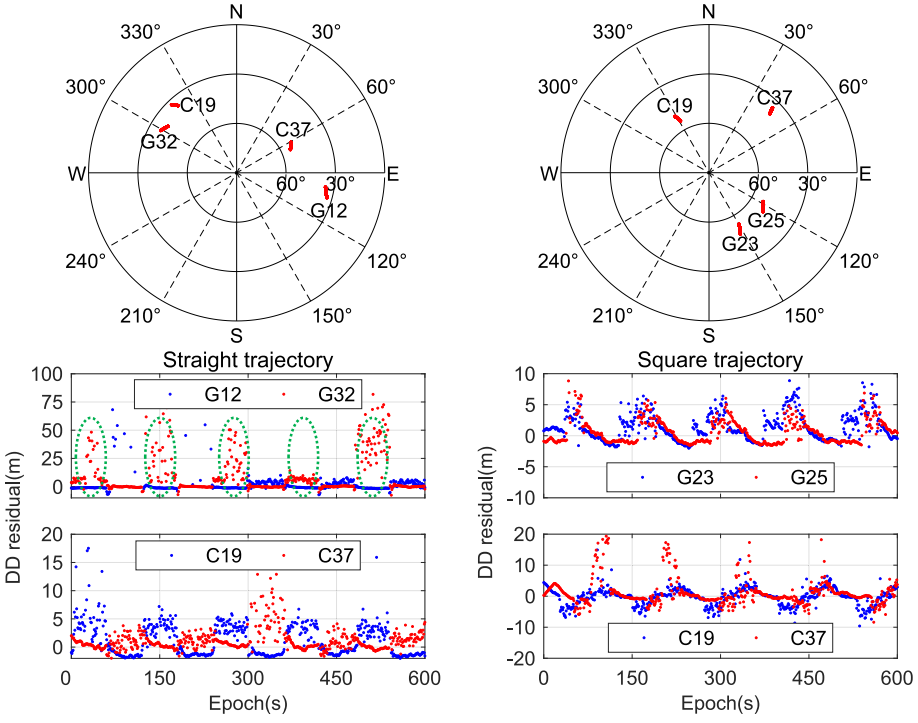

Fig. 3. Sky plot and DD residuals in wrist-mounted scenario of two kinematic tests.

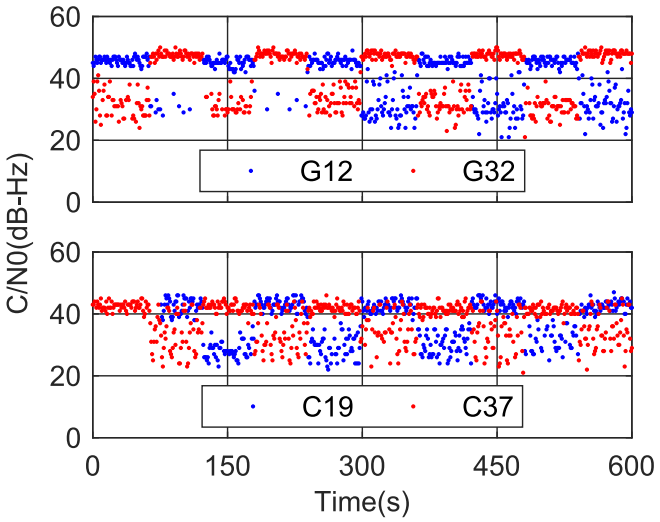

Fig. 4. C/N0 data for the four satellites shown in the left panel of Fig. 3.

where P is the pseudorange observation; ρ is the geometric range from satellite to receiver; ε_P is the measurement noise and other unmodeled errors, such as residual atmospheric and multipath effects; the superscript and subscribe represent satellites and receivers, respectively. For DD calculation, the geodetic GNSS receiver shown in Fig. 1 is used as the base station, while the two INS-Probes equipped with identical antennas serve as the rover stations. Note that if receivers are connected to a common antenna through a signal splitter, ρ_{rb}^{ij} is equal to zero, which is known as zero-baseline approach [19]. In the actual tests, however, the antennas of the base and rover stations are installed at different locations. Since the positions of rover stations cannot be accurately measured in kinematic tests, and the body blockage significantly affects the pseudorange observations, the zero-baseline approach is still adopted here, that is, the errors of DD residuals caused by antenna position differences are ignored.

In the static test, the participant stands still facing east, meaning that the azimuth range within [90°, 270°] corresponds to a shadow region. The sky plot and DD residuals of satellites G12, G23, C08, and C19 in helmet-mounted and wrist-mounted scenarios are shown in Fig. 2. In the wrist-mounted scenario, significant ranging errors are observed for satellites G23 and C08, whereas these satellites perform normally when the antenna is mounted on the helmet. From the sky plot, it can be concluded that satellites G23 and C08 are obstructed by the human body, while satellites G12 and C19 are located in an open-sky area. It is indicated that GNSS body shadowing significantly affects pseudorange observations and cannot be ignored in wrist-worn scenarios. Furthermore, no significant ranging errors are detected when the wrist is fixed in the front position. This is primarily because, at the front-most position (as shown in Fig. 1), the wrist is away from the torso, reducing signal occlusion caused by the body.

The kinematic test was conducted twice: once on the straight route and once on the square route. For each route, the DD residuals of four satellites in wrist-mounted scenario are illustrated in Fig. 3. It can be observed that ranging errors still appear when the participant is under normal walking conditions. When a satellite is not obstructed, the DD

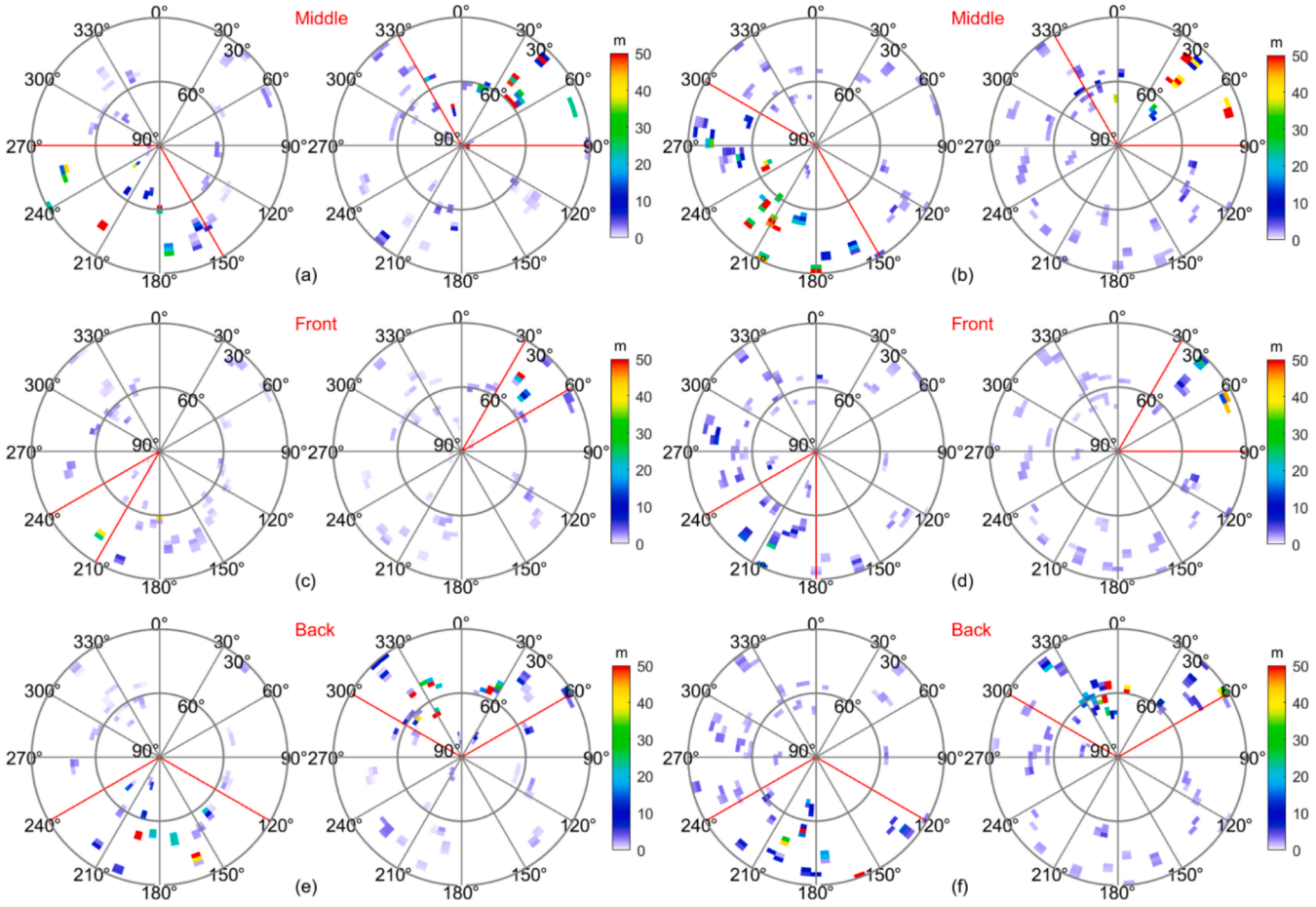

Fig. 5. Distributions of the absolute DD residuals for u-blox F9P and M8U in different wrist positions. The results of u-blox F9P are shown in (a), (c), and (e); the results of u-blox M8U are shown in (b), (d), and (f). Each subgraph contains two panels, which denote east- (left) and west-facing (right) results, respectively.

residuals remain close to zero and exhibit relatively continuous behavior. This is likely due to the filtering methods that have been applied to the output pseudorange observations. However, when a satellite is obstructed, the DD residuals fluctuate significantly, disrupting their continuity. Additionally, since the participant walked back and forth along the predefined route during data collection, the DD residuals exhibit regular patterns. Taking the straight trajectory as an example, a round-trip takes approximately two minutes, and the satellites switch between unobstructed and obstructed states. In total, five round-trips are completed during the test, resulting in each of the four satellites being obstructed five times. This aligns with the circled portions in Fig. 3 (left panel), demonstrating a strong correlation between signal occlusion and ranging error. However, one issue is that the magnitude of ranging errors varies from a few meters to tens of meters, indicating that the shadowing effect on pseudorange observations is difficult to quantify. Therefore, in the subsequent algorithm design, only weight adjustment is applied for the obstructed satellites.

For weight adjustment, it is necessary to find an indicator that can identify the pseudorange quality. Fig. 4 presents the carrier-to-noise density ratio (C/N0) data for the four satellites shown in the left panel of Fig. 3. Without signal occlusion, the C/N0 values range from approximately 40 to 50 dB-Hz in open-sky environment. However, when the satellite is obstructed by human body, a significant decrease (approximately 10–20 dB-Hz) in C/N0 values can be observed. It is evident that periods of DD residual fluctuations align with times when C/N0 values decrease. Nevertheless, in terms of magnitude, there is no clear correlation between the amplitude of DD residuals and the C/N0 values. For instance, in the case of satellite G32, the C/N0 value consistently drops to a similar level each time it is obstructed; but the corresponding DD residuals range from a few meters to tens of meters. These test results suggest that the impacts of GNSS body shadowing on pseudorange observations is complex, which can be influenced by factors such as wrist's swing position and even clothing material. To accurately model the shadowing effects, more detailed studies are required in future work. However, based on the results demonstrated in Fig. 3 and Fig. 4, one conclusion is clear: signal blockage leads to a decrease in C/N0, which is consistent with findings in existing literature. Therefore, once a blocked satellite is detected, C/N0-dependent weighting strategies can be applied to mitigate the impacts of GNSS body shadowing on positioning performance.

2.3. Determination of shadow region

In indoor environments, the propagation conditions of signals are divided into three categories according to azimuth angles [20], namely line-of-sight (LOS), quasi-LOS (QLOS), and non-LOS (NLOS). Similarly, the shadow region caused by human body can also be roughly determined. To identify the shadow region, the absolute DD residuals of pseudorange observations are plotted against azimuth and elevation angles. Specifically, the area with larger residuals is considered to be a shadow region.

However, it is hard work for the participant to perform a long period of data collection (e.g., several hours). Therefore, the static test mentioned earlier (as shown in Fig. 1) is conducted three times in one day, i.e., in the morning, noon, and evening; thus, a richer satellite distribution can be obtained. To assess potential on-device differences, this test utilized two consumer-grade GNSS receivers (i.e., u-blox F9P and M8U) for data collection. For each device, the static tests are conducted for two days: the first day facing east and the second day facing west. Corresponding results are shown in Fig. 5. In order to exclude the environmental impacts, the satellites with elevation angles lower than 30° are discarded in all the tests. It can be seen that the east- and west-facing results of the two devices are basically symmetrical. In addition, it can be found that different shadow regions will be generated when the wrist swings to different positions (the shadow region in each subgraph is indicated by red lines). For instance, it makes sense that the minimal

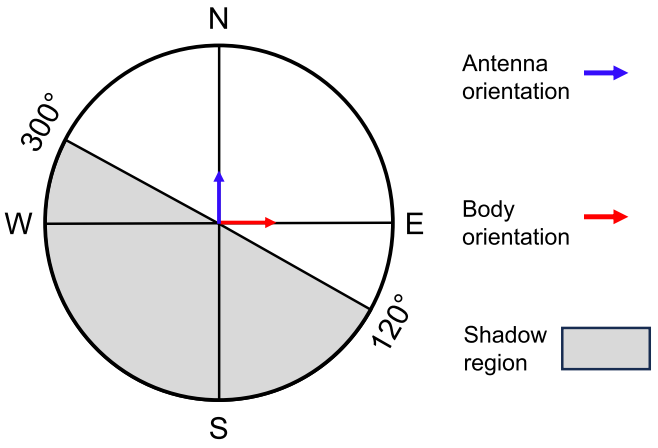

Fig. 6. Determined shadow region when the participant faces east and GNSS antenna attached on left wrist.

impacts can be observed when the wrist is positioned at the forefront (i.e., Fig. 5c and Fig. 5d), which is consistent with the results shown in Fig. 2.

According to the test results shown in Fig. 5, the shadow region can be roughly determined. For example, when the participant faces east and the GNSS antenna attached on left wrist, the azimuth ranges of [150°, 300°] and [120°, 240°] are regarded as shadow regions for Fig. 5b and Fig. 5f, respectively. By taking an intersection of these shadow regions, the final result can be roughly determined, as shown in Fig. 6. Obviously, not all the satellites in the determined region are obstructed by the human body (e.g., Fig. 5c and Fig. 5d); thus, further processing strategy is required and will be described in next section. In addition, to obtain the shadow region, the body orientation (i.e., pedestrian heading) needs be known in advance, which can be provided by PDR. To describe the shadow region in any body orientations, a new variable Δ_φ is defined here:

$$\Delta_\varphi = \varphi_{azi} - \varphi_{heading} \tag{2}$$

where φ_{azi} denotes the azimuth angles of shadow region (i.e., [120°, 300°] in Fig. 6); $\varphi_{heading}$ denotes the pedestrian heading (i.e., 90° in Fig. 6). Then, a fixed range of [30°, 210°] is used to describe the shadow region.

3. Wrist-worn GNSS/INS integrated system

In this section, the system framework of WGINS is first introduced. The proposed algorithm can be divided into two parts: INS-based PDR and tightly-coupled GNSS/INS integration. The detailed steps for each part will be described separately.

3.1. System overview

As shown in Fig. 7, the proposed WGINS adopts a conventional extended Kalman filter (EKF) algorithm framework to fuse single-frequency GPS/BDS observations (pseudorange and Doppler) and six-axis micro-electro-mechanical-system (MEMS) IMU (three-axis gyroscope and three-axis accelerometer) measurements. Two key points are summarized for WGINS: 1) a strapdown INS-based PDR system is specifically designed for wrist-worn inertial sensors, and high-frequency position and attitude information can be obtained; 2) according to the prior information provided by PDR and the determined shadow region, the obstructed satellites can be detected, which are subsequently down-weighted with corresponding weighting strategies to mitigate the impacts of GNSS body shadowing. Note that motion recognition has not been considered in this paper, namely, the proposed algorithm works

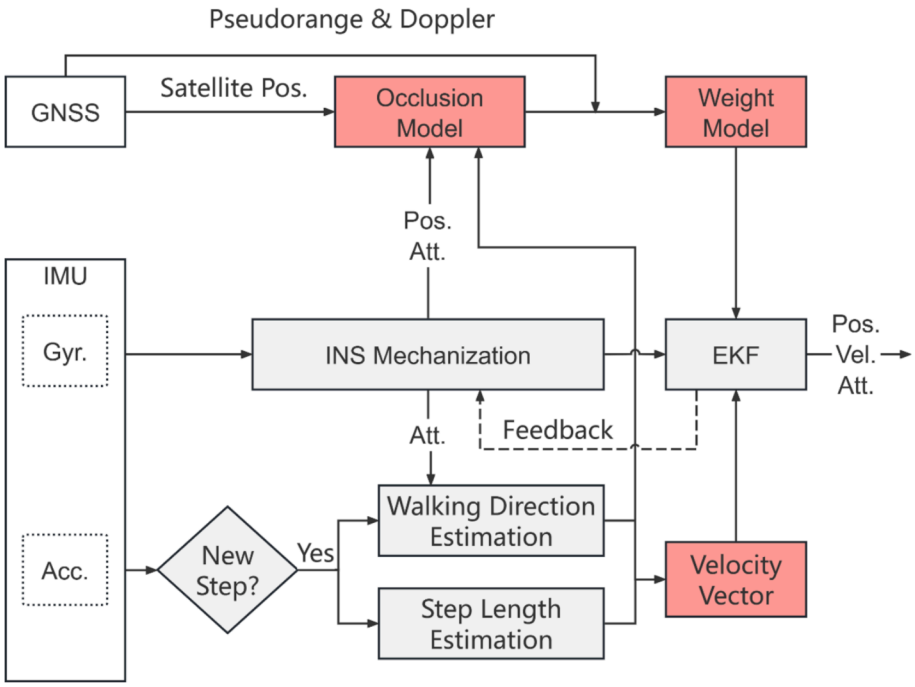

Fig. 7. System framework for WGINS. The red blocks denote the proposed works in this paper.

Fig. 8. Illustration of the defined b-frame (red arrows) and h-frame (blue arrows).

under normal arm swinging conditions.

The coordinate systems used in this paper are briefly introduced below. In addition to the conventional earth-centered-earth-fixed-frame (e-frame) and navigation-frame (n-frame, pointing to north-east-down), body-frame (b-frame) and human-frame (h-frame) are defined as shown in Fig. 8. When the INS-Probe is tied to the wrist, the X-axis of the b-frame points to the lateral side of the human body. For the h-frame, the origin is set at the shoulder and the X-axis is parallel to the walking direction. Note that there is a mounting angle between the b-frame and h-frame, which should be estimated in real-time to obtain the walking direction.

3.2. INS-based PDR

The prior information (i.e., position and attitude) provided by PDR is the basis for WGINS to work. Traditional step-model-based PDR algorithms estimate the user's position using step length and walking direction, updating the position only when a step is detected. This results in a relatively low output frequency (e.g., around 2 Hz). Additionally, such methods are unable to provide attitude information, making it impossible to capture the actual dynamics of arm swinging. Therefore, an INS-based PDR method that is specifically designed for wrist-worn inertial sensors is proposed.

3.2.1. INS mechanization

After initialization, INS can output continuous and high-frequency position, velocity, and attitude (PVA) results by utilizing the specific force and angular rate measurements provided by the embedded accelerometer and gyroscope, which is known as INS mechanization. After neglecting the small terms of error correction, the equations can be written as [21]:

$$\begin{cases} \boldsymbol{r}_k^n = \boldsymbol{r}_{k-1}^n + \boldsymbol{v}_k^n \Delta t \\ \boldsymbol{v}_k^n = \boldsymbol{v}_{k-1}^n + \left[\boldsymbol{C}_{b,k}^n \left(\boldsymbol{f}_k^b - \boldsymbol{b}_a \right) + \boldsymbol{g}^n \right] \Delta t \\ \boldsymbol{q}_{b,k}^n = \boldsymbol{q}_{b,k-1}^n \otimes \boldsymbol{q} \left[\left(\boldsymbol{\omega}_k^b - \boldsymbol{b}_g \right) \Delta t \right] \end{cases} \tag{3}$$

where $\boldsymbol{r}^n$ and $\boldsymbol{v}^n$ represent the position and velocity vector in the n-frame, respectively; $\boldsymbol{C}_b^n$ is the rotation matrix from the b-frame to the n-frame; $\boldsymbol{f}^b$ and $\boldsymbol{\omega}^b$ represent the acceleration and angle rate measurement vector in the b-frame, respectively; $\boldsymbol{b}_a$ and $\boldsymbol{b}_g$ refer to the bias vector of the tri-accelerometer and tri-gyroscope, respectively; $\boldsymbol{g}^n$ is the local gravity vector in the n-frame; quaternion $\boldsymbol{q}_b^n$ denotes the rotation of the

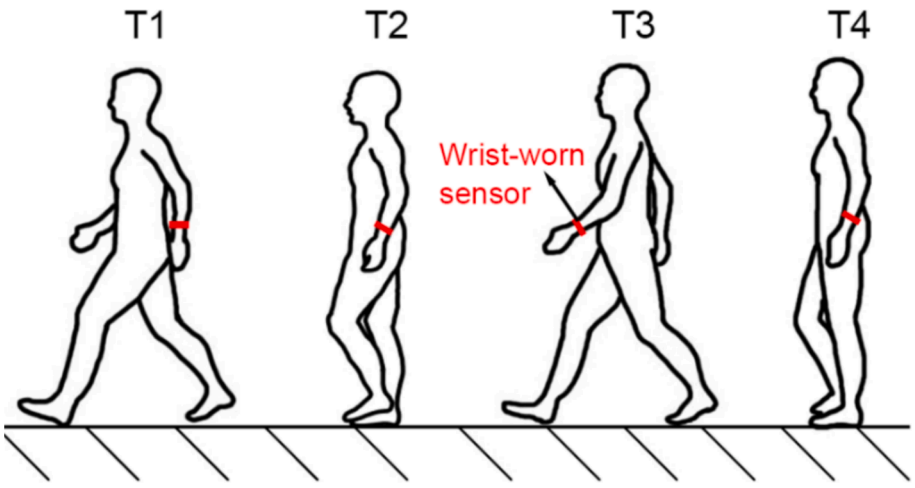

Fig. 9. Diagram of arm swinging for pedestrian under normal walking conditions.

b-frame with respect to the n-frame; $\otimes$ denotes the quaternion product; Δt is the time interval between the k-th epoch and (k-1)-th epoch.

3.2.2. Filter design

Although INS can provide continuous PVA solutions after initialization, its error can be rapidly accumulated in a very short time (a few seconds) by using the low-cost inertial sensors embedded in smart devices. Therefore, EKF is usually employed to fuse INS with other navigation sources. The 19-dimensional error state vector $\delta \boldsymbol{x}_{INS}$ is defined as:

$$\delta \boldsymbol{x}_{INS} = \begin{bmatrix} \delta \boldsymbol{r}^n & \delta \boldsymbol{v}^n & \boldsymbol{\varphi} & \delta \boldsymbol{b}_g & \delta \boldsymbol{b}_a & \delta \boldsymbol{l}^b & \delta \kappa \end{bmatrix}^T \tag{4}$$

where $\delta \boldsymbol{r}^n$, $\delta \boldsymbol{v}^n$, $\boldsymbol{\varphi}$, $\delta \boldsymbol{b}_g$, and $\delta \boldsymbol{b}_a$ represent the error vectors of position, velocity, attitude, gyroscope bias, and accelerometer bias, respectively; $\delta \boldsymbol{l}^b$ refers to the error vector of level-arm in the b-frame, which cannot be neglected in wrist-worn scenarios and will be explained in subsequent part; $\delta \kappa$ is the scale error of step length. Then, the state and observation equations can be expressed as:

$$\begin{cases} \delta \boldsymbol{x}_{k,k-1} = \boldsymbol{\Phi}_{k-1} \delta \boldsymbol{x}_{k-1,k-1} + \boldsymbol{w}_k \\ \delta \boldsymbol{z}_k = \boldsymbol{H}_k \delta \boldsymbol{x}_{k,k-1} + \boldsymbol{\varepsilon}_k \end{cases} \tag{5}$$

where $\delta \boldsymbol{x}_{k-1,k-1}$ and $\delta \boldsymbol{x}_{k,k-1}$ represent the previous and predicted error state vector, respectively; $\delta \boldsymbol{z}_k$ and $\boldsymbol{H}_k$ are the measurement vector and the design matrix, respectively; $\boldsymbol{w}_k$ and $\boldsymbol{\varepsilon}_k$ denote the process noise and measurement noise, respectively; $\boldsymbol{\Phi}_{k-1}$ is the 19 $\times$ 19 state transition matrix:

$$\boldsymbol{\Phi}_{k-1} = \begin{bmatrix} \boldsymbol{I}_{3\times3} & \boldsymbol{I}_{3\times3}\Delta t & \boldsymbol{0}_{3\times3} & \boldsymbol{0}_{3\times3} & \boldsymbol{0}_{3\times3} & \boldsymbol{0}_{3\times4} \\ \boldsymbol{0}_{3\times3} & \boldsymbol{I}_{3\times3} & (\boldsymbol{f}_k^n \times)\Delta t & \boldsymbol{0}_{3\times3} & \boldsymbol{C}_{b,k}^n \Delta t & \boldsymbol{0}_{3\times4} \\ \boldsymbol{0}_{3\times3} & \boldsymbol{0}_{3\times3} & \boldsymbol{I}_{3\times3} & -\boldsymbol{C}_{b,k}^n \Delta t & \boldsymbol{0}_{3\times3} & \boldsymbol{0}_{3\times4} \\ \boldsymbol{0}_{3\times3} & \boldsymbol{0}_{3\times3} & \boldsymbol{0}_{3\times3} & \boldsymbol{I}_{3\times3} & \boldsymbol{0}_{3\times3} & \boldsymbol{0}_{3\times4} \\ \boldsymbol{0}_{3\times3} & \boldsymbol{0}_{3\times3} & \boldsymbol{0}_{3\times3} & \boldsymbol{0}_{3\times3} & \boldsymbol{I}_{3\times3} & \boldsymbol{0}_{3\times4} \\ \boldsymbol{0}_{4\times3} & \boldsymbol{0}_{4\times3} & \boldsymbol{0}_{4\times3} & \boldsymbol{0}_{4\times3} & \boldsymbol{0}_{4\times3} & \boldsymbol{I}_{4\times4} \end{bmatrix} \tag{6}$$

3.2.3. Pedestrian motion constraint

For pedestrian under normal walking conditions, a basic assumption is that the speed is only in the forward direction, and the lateral and vertical velocity is equal to zero [21], which is known as pedestrian motion constraint. However, the wrist movements are uncoupled with human body, so the wrist speed is not consistent with body speed. To address this issue, the level-arm described in (4) is estimated in real-time to compensate for the velocity discrepancy.

As illustrated in Fig. 9, the wrist swings to different positions when the pedestrian under normal walking conditions. However, the lowest point (i.e., T2 and T4 in Fig. 9) remains stable relative to the human body, which reflects the pedestrian's position more accurately. Besides, when the wrist swings to the lowest point, the whole arm is close to be straight. At this moment, the arm swinging is modeled as a single pendulum motion, and the body speed can be expressed as:

$$\boldsymbol{v}_{body} = \boldsymbol{v}_{wrist} + \boldsymbol{\omega} \times \boldsymbol{l} \tag{7}$$

where $\boldsymbol{v}_{wrist}$ denotes the wrist speed provided by INS; $\boldsymbol{\omega}$ is the angle rate of arm swinging, which can be approximately provided by the mounted inertial sensor (i.e., the whole arm is regarded as a rigid body); $\times$ denotes the cross product; $\boldsymbol{l}$ is the level-arm from wrist to shoulder (i.e., the origin of the defined h-frame). Based on this rule, the pedestrian motion constraint can be used more accurate by considering level-arm compensation. Note that different users have different arm lengths, so the level-arm is considered in filter design and estimated in real-time.

Fortunately, the lowest point can be caught via step detection. In general, the norm of tri-accelerometer measurements is used for step detection, which can be written as:

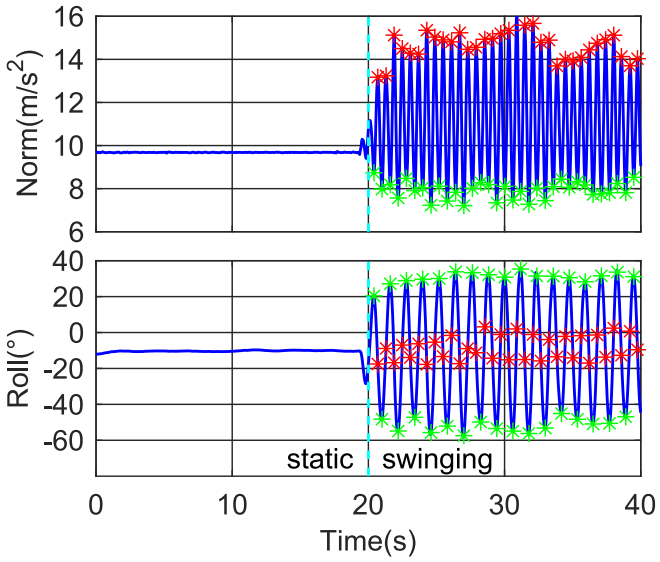

Fig. 10. The norm of tri-accelerometer measurements and corresponding roll angles for detected steps. The red and green asterisks denote detected steps using signal peaks and valleys, respectively.

$$acc_{norm} = \sqrt{acc_x^2 + acc_y^2 + acc_z^2} \tag{8}$$

where acc_x, acc_y, and acc_z denote the tri-accelerometer measurements. The signal peak or valley of the accumulated features in the detection window is counted as a step [17], as shown in Fig. 10 (top panel). Referring to the b-frame illustrated in Fig. 8, roll angle is associated with arm swinging, so corresponding roll angles for step detection using signal peaks and valleys are shown in Fig. 10 (bottom panel). In static state, the wrist is fixed to the lateral side of human body, and the roll angles are around -10°. In swinging state, the roll angles of detected steps using signal peaks are close to that of static state, which verifies that the lowest point can be caught by using signal peak to detect step. In addition, the roll angle shown in Fig. 10 serves an additional purpose, namely, recognizing whether the device is worn on the left or right hand. Specifically, the roll angles close to 0° indicates that the device is worn on the left hand, while the roll angles near $\pm 180^\circ$ suggests it is worn on the right hand.

When a step detected, the pedestrian velocity in the h-frame can be written as:

$$\widetilde{\boldsymbol{v}}^h = \begin{bmatrix} (\kappa + \delta\kappa)SL/\Delta t & 0 & 0 \end{bmatrix}^T + \boldsymbol{\varepsilon}_v \tag{9}$$

where κ is the scale of step length; SL is the step length, which can be estimated via an empirical formula [22]; Δt is the time interval between two adjacent steps; $\boldsymbol{\varepsilon}_v$ denotes the observation noise. According to (7), the pedestrian velocity derived from INS can be modeled as:

$$\boldsymbol{v}^h = \boldsymbol{C}_b^h \boldsymbol{C}_n^b \boldsymbol{v}^n + \boldsymbol{C}_b^h (\boldsymbol{\omega}^b \times) \boldsymbol{l}^b \tag{10}$$

The velocity vector, accounting for the error terms, can then be expressed as:

$$\begin{aligned} \widehat{v}^h &= \boldsymbol{C}_b^h \boldsymbol{C}_n^b (\boldsymbol{I} + \boldsymbol{\varphi} \times)(\boldsymbol{v}^n + \delta\boldsymbol{v}^n) + \boldsymbol{C}_b^h \left((\boldsymbol{\omega}^b + \delta\boldsymbol{b}_g) \times\right)\left(\boldsymbol{l}^b + \delta\boldsymbol{l}^b\right) \\ &\approx \boldsymbol{v}^h + \boldsymbol{C}_b^h \boldsymbol{C}_n^b \delta\boldsymbol{v}^n - \boldsymbol{C}_b^h \boldsymbol{C}_n^b (\boldsymbol{v}^n \times)\boldsymbol{\varphi} - \boldsymbol{C}_b^h \left(\boldsymbol{l}^b \times\right)\delta\boldsymbol{b}_g + \boldsymbol{C}_b^h (\boldsymbol{\omega}^b \times)\delta\boldsymbol{l}^b \end{aligned} \tag{11}$$

where C_b^h denotes the rotation matrix from the b-frame to the h-frame. To obtain $\boldsymbol{C}_b^h$, the mounting angle (as illustrated in Fig. 8) needs to be estimated in advance. Typically, the principal component analysis (PCA) method is employed [23], which assumes that the principal direction of arm swinging can reflect the pedestrian heading. After mounting angle is estimated, the pedestrian heading can be expressed as:

$$\varphi_{heading} = \varphi_{INS} - \varphi_{mount} \tag{12}$$

where φ_{INS} is the sensor heading; φ_{mount} is the mounting angle. The observation equation can be written as:

$$\begin{aligned} \delta\boldsymbol{z}_v &= \widehat{\boldsymbol{v}}^h - \widetilde{\boldsymbol{v}}^h \\ &= \boldsymbol{C}_b^h \boldsymbol{C}_n^b \delta\boldsymbol{v}^n - \boldsymbol{C}_b^h \boldsymbol{C}_n^b (\boldsymbol{v}^n \times)\boldsymbol{\varphi} - \boldsymbol{C}_b^h \left(\boldsymbol{l}^b \times\right)\delta\boldsymbol{b}_g + \\ &\quad \boldsymbol{C}_b^h (\boldsymbol{\omega}^b \times)\delta\boldsymbol{l}^b - \boldsymbol{v}_{step}\delta\kappa + \boldsymbol{\varepsilon}_v \end{aligned} \tag{13}$$

where $\boldsymbol{v}_{step} = \begin{bmatrix} SL/\Delta t & 0 & 0 \end{bmatrix}^T$. Finally, the detailed procedure of the proposed INS-based PDR algorithm is outlined in Algorithm 1.

Algorithm 1: Procedure of the proposed INS-based PDR algorithm

```
Input: Six-axis IMU measurements
       GNSS positioning results
Output: High-frequency (e.g., 100 Hz) PVA results
Step1: Initialize the state vector of INS
Step2: INS mechanization using IMU measurements
Step3: if step detected
         Estimate step length using empirical formula
         Estimate walking direction using PCA
         KF update based on pedestrian motion constraint
       end if
Repeat steps 2–3 until the data is fully processed
```

3.3. Tightly-coupled GNSS/INS integration

GNSS/INS integration is the most common positioning solution adopted in outdoor environments. As the tightly-coupled algorithm uses raw GNSS observations, each satellite can be analyzed individually. Therefore, if the obstructed satellites can be detected, lower weights can be assigned to these satellites and the impacts of GNSS body shadowing can be effectively mitigated.

3.3.1. GNSS observations

To fuse GNSS and INS in tightly-coupled mode, the error state vector needs to be extended:

$$\delta\boldsymbol{x} = \begin{bmatrix} \delta\boldsymbol{x}_{INS} \\ \delta\boldsymbol{x}_{GNSS} \end{bmatrix} \tag{14}$$

where $\delta\boldsymbol{x}_{INS}$ can be found in (4); $\delta\boldsymbol{x}_{GNSS} = \begin{bmatrix} t_{bias}^g & t_{bias}^c & t_{drift} \end{bmatrix}^T$; t_{bias}^g and t_{bias}^c are the clock bias of GPS and BDS, respectively; t_{drift} is the clock drift. The 22×22 state transition matrix is written as:

$$\boldsymbol{\Phi}_{22\times22} = \begin{bmatrix} \boldsymbol{\Phi}_{19\times19} & 0_{19\times1} & 0_{19\times1} & 0_{19\times1} \\ 0_{1\times19} & 1 & 0 & \Delta t \\ 0_{1\times19} & 0 & 1 & \Delta t \\ 0_{1\times19} & 0 & 0 & 1 \end{bmatrix} \tag{15}$$

where $\boldsymbol{\Phi}_{19\times19}$ can be found in (6).

In this paper, single-frequency pseudorange and pseudorange rate (derived from Doppler observations) are used. Utilizing the position provided by INS, the pseudorange and pseudorange rate can be written as:

$$\begin{cases} \widetilde{P} = \rho_{INS} - \boldsymbol{l}_{INS}^e \cdot \delta\boldsymbol{r}^e + c\delta t_r + \varepsilon_P \\ \widetilde{\dot{P}} = \boldsymbol{l}_{INS}^e \cdot (\boldsymbol{v}_r^e - \boldsymbol{v}_s^e) + c\dot{\delta} t_r + \varepsilon_{\dot{P}} \end{cases} \tag{16}$$

where $\widetilde{P}$ denotes the raw pseudorange observations that considering satellite clock bias and atmospheric effects elimination; $\widetilde{\dot{P}}$ is the pseudorange rate derived from Doppler observations; ρ_{INS} is the geometric range from satellite to INS position; $\delta\boldsymbol{r}^e$ is the position error vector in the e-frame; $\boldsymbol{v}_r^e$ and $\boldsymbol{v}_s^e$ represent the true velocity of receiver and satellite in the e-frame, respectively; $c\delta t_r$ is the receiver clock bias in meter; $c\dot{\delta} t_r$ is the receiver clock drift in meter per second; ε_P and $\varepsilon_{\dot{P}}$ are the observation errors; $\boldsymbol{l}_{INS}^e$ is the LOS unit vector from satellite to INS position in the e-frame, which can be written as:

$$\boldsymbol{l}_{INS}^e = \frac{\boldsymbol{r}_{INS}^e - \boldsymbol{r}_s^e}{\rho_{INS}} = \frac{\boldsymbol{r}_{INS}^e - \boldsymbol{r}_s^e}{\left\| \boldsymbol{r}_{INS}^e - \boldsymbol{r}_s^e \right\|} \tag{17}$$

where $\boldsymbol{r}_{INS}^e$ and $\boldsymbol{r}_s^e$ denote the INS position and satellite position in the e-frame.

The pseudorange and pseudorange rate derived from INS can be expressed as:

$$\begin{cases} \widehat{P} = \rho_{INS} \\ \widehat{\dot{P}} = \boldsymbol{l}_{INS}^e \cdot (\boldsymbol{v}_{INS}^e - \boldsymbol{v}_s^e) \end{cases} \tag{18}$$

where $\boldsymbol{v}_{INS}^e = \boldsymbol{v}_r^e + \delta\boldsymbol{v}^e$ denotes the INS velocity in the e-frame. Finally, the observation equations can be written as:

$$\begin{cases} \delta z_P = \widehat{P} - \widetilde{P} = \boldsymbol{l}_{INS}^e \cdot \delta\boldsymbol{r}^e - c\delta t_r + \varepsilon_P \\ \delta z_{\dot{P}} = \widehat{\dot{P}} - \widetilde{\dot{P}} = \boldsymbol{l}_{INS}^e \cdot \delta\boldsymbol{v}^e - c\dot{\delta} t_r + \varepsilon_{\dot{P}} \end{cases} \tag{19}$$

Note that $\delta\boldsymbol{r}^e$ and $\delta\boldsymbol{v}^e$ represent error vectors in the e-frame, which should be converted to the n-frame:

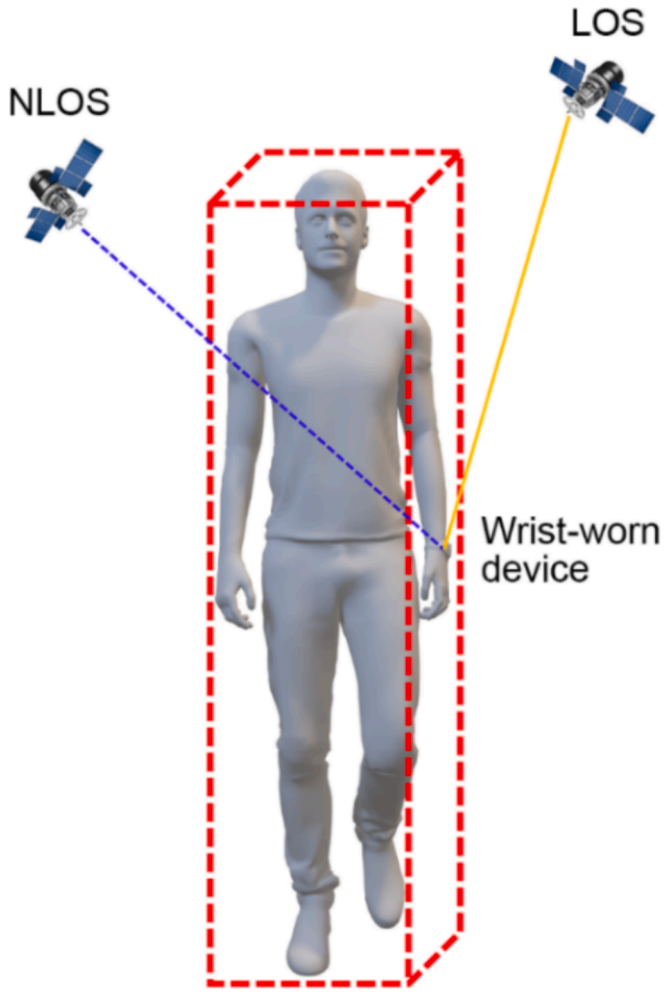

Fig. 11. Diagram of the GNSS signal occlusion caused by human body.

$$\begin{cases} \delta \boldsymbol{r}^e = \boldsymbol{C}_n^e \delta \boldsymbol{r}^n \\ \delta \boldsymbol{v}^e = \boldsymbol{C}_n^e \delta \boldsymbol{v}^n \end{cases} \tag{20}$$

where $\boldsymbol{C}_n^e$ is the rotation matrix from the n-frame to the e-frame.

3.3.2. Occlusion model

As described above, if the obstructed satellites can be detected, corresponding weighting strategies can be adopted to mitigate the impacts of GNSS body shadowing. Therefore, the occlusion model mentioned in Fig. 7 is introduced here. As shown in Fig. 6, a shadow region can be roughly determined after pedestrian heading is provided by INS-based PDR. In addition, the azimuth angle of satellite φ_{sat} can be calculated by using satellite position and INS position. According to (2) and (12), whether a satellite is in the shadow region can be determined by the following formula:

$$\varphi_{sat} - \varphi_{heading} \in \Delta\varphi \tag{21}$$

However, not all the satellites in the shadow region are obstructed by human body, so a secondary judgment is necessary to be considered.

Fig. 11 demonstrates the GNSS signal occlusion caused by human body. In this paper, the human body is simply modeled as a cuboid, and the LOS and NLOS satellites can be distinguished by judging whether the LOS vector (from wrist to satellite) passes through the human body. To simplify the calculations, the INS position and the satellite position are converted to the h-frame:

$$\begin{cases} \boldsymbol{r}_{INS}^h = \boldsymbol{r}_{INS,0}^h + \boldsymbol{C}_b^h \boldsymbol{C}_n^b \Delta \boldsymbol{r}_{INS}^n \\ \boldsymbol{r}_s^h = \boldsymbol{C}_b^h \boldsymbol{C}_n^b \boldsymbol{C}_e^n \left(\boldsymbol{r}_s^e - \boldsymbol{r}_{origin}^e \right) \end{cases} \tag{22}$$

where $\boldsymbol{r}_{INS,0}^h$ is the INS position at last step-detected moment, which can be obtained after estimating the level-arm; $\Delta \boldsymbol{r}_{INS}^n$ denotes the position variation from last step-detected moment to current epoch; $\boldsymbol{r}_s^e$ and $\boldsymbol{r}_{origin}^e$ represent the satellite position and the origin position of h-frame in the e-frame, respectively. Then, the LOS vector in the h-frame can be easily calculated. Finally, a simple collision detection algorithm is implemented to judge whether the satellite is occluded by human body.

In summary, three cases are considered in the proposed occlusion model: 1) satellite in open-sky area; 2) satellite in the determined shadow region but the LOS vector is not obstructed by human body; 3) satellite in the determined shadow region and the LOS vector is obstructed by human body. Different weighting strategies will be adopted for different cases.

3.3.3. Weighting strategy

In KF model, the precision of observations is described by the measurement noise matrix $\boldsymbol{R}$, which can be written as:

$$\boldsymbol{R} = diag\left(\sigma_1^2 \quad \sigma_2^2 \quad \cdots \quad \sigma_n^2 \right) \tag{23}$$

where σ^2 is the observation variance; n denotes the number of observations. Generally, the abnormal observations are down-weighted so that their impacts on final results can be mitigated. Considering the impacts of GNSS body shadowing, the variance of the k-th observation is defined as:

$$\sigma_k^2 = \sigma_{obs}^2 + \sigma_{eph}^2 + \sigma_{ion}^2 + \sigma_{trop}^2 + \sigma_{body}^2 \tag{24}$$

where σ_{obs}^2, σ_{eph}^2, σ_{ion}^2, and σ_{trop}^2 are the variances of measurement noise, satellite related errors, ionosphere error, and troposphere error, respectively; σ_{body}^2 denotes the impacts caused by GNSS body shadowing.

As the shadowing effect on pseudorange observations is difficult to be quantified, thus an empirical model is used here. Associated with the three cases mentioned in occlusion model, σ_{body} is assigned with different values. For case1, the pseudorange observation is not affected by human body, thus σ_{body} is set to 0. For case2, since C/N0 data can identify the pseudorange quality (as illustrated in Fig. 4), a C/N0-dependent weighting strategy is adopted. For case3, the satellite is completely obstructed by human body, so the observation is discarded. Specifically, σ_{body} is written as:

$$\sigma_{body} = \begin{cases} 0, case1 \\ k_0 * 10^{\frac{\max(CNMAX - C/N0, 0)}{10}}, case2 \\ 10^6, case3 \end{cases} \tag{25}$$

where k_0 is an experience factor; $\max(\cdot)$ is the maximum function; $CNMAX$ is a constant value set to 40 dB-Hz [24].

In addition to the weight model, the Institute of Geodesy and Geophysics III (IGG III) weight function is also employed [25]. The IGG III weight function uses a variance expansion factor λ_i to mitigate the impacts caused by gross errors, which is modeled as [26]:

$$\frac{1}{\lambda_i} = \begin{cases} 1, \omega_i \le k_0 \\ \frac{k_0}{\omega_i} \times \left(\frac{k_1 - \omega_i}{k_1 - k_0} \right)^2, k_0 < \omega_i \le k_1 \\ 10^{-6}, \omega_i > k_1 \end{cases} \tag{26}$$

where k_0 and k_1 are two empirical thresholds; ω_i is the standardized innovation value:

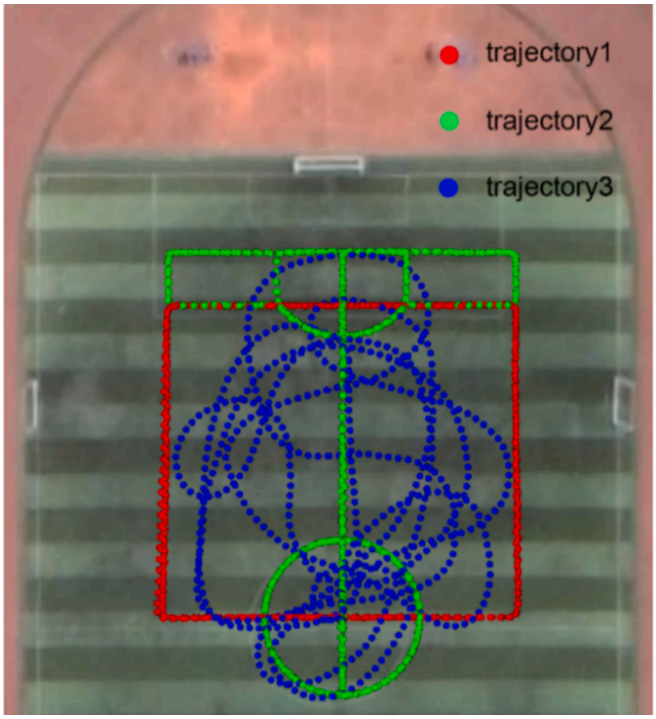

Fig. 12. Test trajectories for performance evaluation.

$$\omega_i = \frac{|v_i|}{\sigma_{v_i}} \tag{27}$$

where v_i and σ_{v_i} denote the innovation value and the corresponding STD. The final measurement noise matrix can be written as:

$$\overline{\boldsymbol{R}}_{ii} = \lambda_i \boldsymbol{R}_{ii} \tag{28}$$

Finally, the detailed procedure of the shadowing effects mitigation algorithm is presented in Algorithm 2.

Algorithm 2: Procedure of the shadowing effects mitigation algorithm

Input: GNSS raw observations (pseudorange and Doppler)
Navigation ephemeris
Position and attitude results provided by INS-based PDR
Output: PVA results
Step1: Occlusion classification based on the occlusion model
Case1: in open-sky area
Case2: in shadow region
Case3: LOS vector passes through the human body
Step2: Weight adjustment based on (24), (25) and (26)
Step3: KF update using GNSS observations

4. Test results and analysis

In this section, three types of positioning results are analyzed, including single GNSS positioning, PDR positioning, and GNSS/PDR integrated positioning. The GNSS positioning results are derived from the data collected in Section 2.3. In the static state, obstructed satellites can be accurately identified, allowing for an analysis of the impact of shadowing effects. The PDR and GNSS/PDR positioning results are based on data collected using the equipment shown in Fig. 8. For performance evaluation, three participants were involved in data collection, and three test trajectories are designed as shown in Fig. 12. The first trajectory is a simple rectangular route; the second trajectory is more complex and consists of rectangular and curved routes; the third trajectory is generated by random movement. Each trajectory takes about 10 min to walk, namely, one participant collects 30 min of test data. In addition, the reference results are provided by the geodetic GNSS receiver with ambiguity-fixed RTK solution.

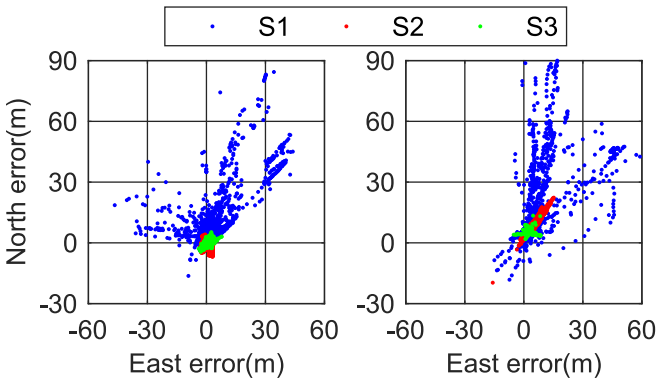

Fig. 13. Horizontal positioning errors of different SPP solutions.

4.1. GNSS positioning performance analysis

In Section 2.3, the shadow region is determined using the static GNSS observations. In this case, GNSS positioning results can be analyzed by excluding observations from obstructed satellites. To evaluate the impacts of GNSS body shadowing on positioning performance, three solutions solved by RTKLIB are compared: (1) antenna mounted on the wrist (S1); (2) antenna mounted on the wrist with the obstructed satellites removed (S2); (3) antenna mounted on the helmet (S3).

The horizontal positioning errors for two datasets, each lasting approximately 30 min, are shown in Fig. 13. To eliminate environmental effects, only satellites with elevation angles greater than 30° are considered in the calculation. The results clearly show that body shadowing significantly degrades GNSS positioning accuracy in S1. Furthermore, the positioning errors are predominantly biased toward the north, primarily due to the obstructed satellites being located in the south in both datasets. When the obstructed satellites are manually excluded (S2), the positioning performance improves considerably. However, it still falls slightly short of the accuracy achieved with the helmet-mounted antenna (S3). This is mainly because removing satellites degrades the satellite geometry, which in turn affects the final positioning performance. Overall, these results demonstrate that GNSS body shadowing has a substantial impact on positioning accuracy and should be further considered in algorithm design for integrated navigation systems.

4.2. Positioning performance analysis of wrist-worn PDR

The position and attitude provided by INS-based PDR are key factors for occlusion model to work properly. Therefore, the positioning performance of two PDR methods is analyzed: 1) conventional INS-based PDR (M1); 2) the proposed wrist-worn INS-based PDR considering level-arm (M2). The test trajectories of the first participant (P1) are shown in Fig. 14. Note that the INS-based PDR can output high-frequency PVA results, but for consistency, only the results at step-detected moments are used for evaluation.

From Fig. 14, it can be seen that heading drift is the main factor that is affecting positioning performance, which is unavoidable for PDR methods. The horizontal position errors of the two PDR methods are summarized in Table 1. Three statistics are used in this paper, including root-mean-square (RMS), circular-error-probable (CEP) 68, and CEP95. The average values of the three statistics are 6.71 m, 7.53 m, and 11.38 m for M1; 4.88 m, 5.17 m, and 8.82 m for M2. Since the magnetometer is not currently used in the proposed algorithm, the heading accuracy cannot be guaranteed for the two PDR methods; however, the pedestrian motion constraint can suppress the heading drift to a certain extent.

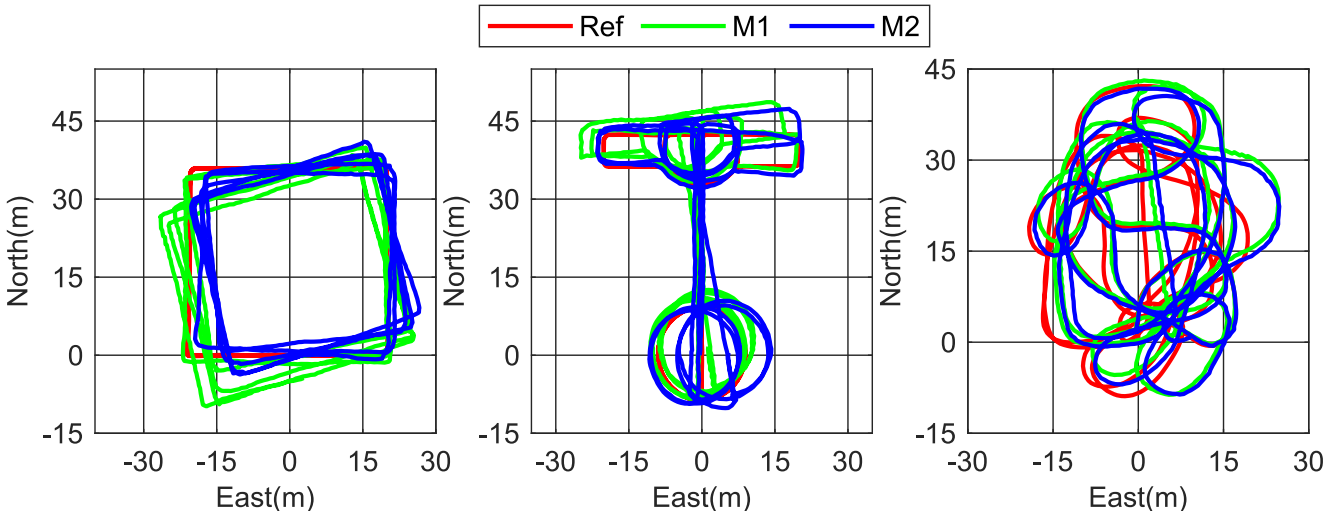

Fig. 14. Trajectories of two INS-based PDR methods for one participant.

Table 1
Statistical results of horizontal position errors for two INS-based PDR methods (unit: m).

		M1			M2		
		RMS	CEP68	CEP95	RMS	CEP68	CEP95
P1	Test1	5.83	6.37	10.58	5.45	6.28	9.71
	Test2	3.36	3.52	6.38	2.94	2.48	6.29
	Test3	4.20	3.60	8.27	4.22	3.74	8.07
P2	Test1	7.27	8.81	11.91	5.93	6.48	10.99
	Test2	6.27	7.28	8.35	6.69	7.76	10.62
	Test3	5.84	7.11	9.96	4.07	4.54	7.70
P3	Test1	6.08	6.73	10.27	5.11	5.74	8.63
	Test2	10.82	12.35	17.86	5.12	5.59	8.21
	Test3	10.70	12.01	18.85	4.38	3.95	9.11
Mean		6.71	7.53	11.38	4.88	5.17	8.82

While the motion assumption may not be satisfied if the level-arm is ignored in wrist-worn scenarios, and low-precision positioning results could be obtained when using inaccurate correction information, which explains why the test results of M2 are better than those of M1, and approximately 27 % of improvement has been achieved in terms of RMS.

4.3. Positioning performance analysis of WGINS

To evaluate the positioning performance of the proposed WGINS, two types of strategies are compared: 1) conventional GNSS/INS integration ignoring the impacts of GNSS body shadowing (W1); 2) the proposed WGINS (W2). The test trajectories for one participant are shown in Fig. 15. In wrist-worn mode, the two tightly-coupled solutions

Table 2
Statistical results of horizontal position errors for the two integrated methods (unit: m).

		W1			W2		
		RMS	CEP68	CEP95	RMS	CEP68	CEP95
P1	Test1	2.23	2.49	3.55	1.23	1.33	2.01
	Test2	1.84	2.01	2.96	1.40	1.44	2.36
	Test3	1.83	2.00	2.80	1.32	1.48	1.85
P2	Test1	2.59	2.70	4.53	1.33	1.49	2.23
	Test2	1.38	1.53	2.26	1.17	1.28	1.84
	Test3	1.58	1.68	2.66	1.43	1.47	2.42
P3	Test1	3.65	4.21	5.59	2.48	2.79	3.81
	Test2	3.17	3.56	5.15	2.49	2.69	3.71
	Test3	3.51	4.21	5.43	2.53	2.95	3.69
Mean		2.42	2.71	3.88	1.71	1.88	2.66

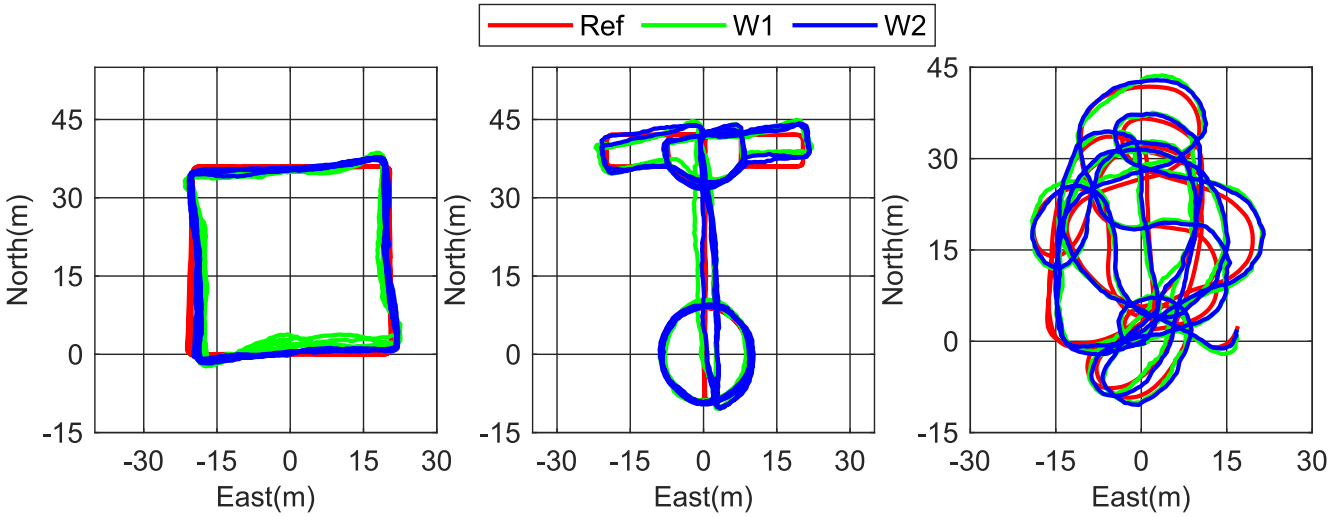

Fig. 15. Trajectories of the methods ignoring (W1) and considering (W2) GNSS body shadowing.

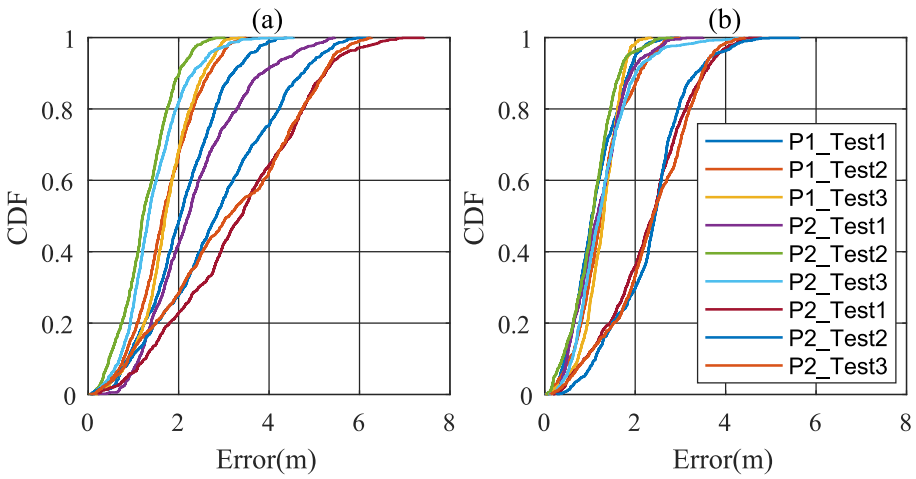

Fig. 16. CDF of the two integrated methods in all the tests. (a) W1; (b) W2.

perform much better than the results shown in Fig. 13, which verifies that combining GNSS with INS-based PDR can effectively improve the positioning accuracy. Moreover, it is observed that the positioning accuracy can be further improved after considering GNSS body shadowing effects, indicating that the proposed algorithm is effective to a certain extent.

Corresponding RMS, CEP68, and CEP95 of horizontal position errors are summarized in Table 2; besides, the cumulative distribution function (CDF) of the two solutions in all the tests is shown in Fig. 16. The average values of the three statistics are 2.42 m, 2.71 m, and 3.88 m for W1; 1.71 m, 1.88 m, and 2.66 m for W2. After comparing the statistical results, it is found that there is no significant improvement in positioning performance, and approximately 29 % improvement has been achieved in terms of RMS for the proposed algorithm. Benefit from the GNSS/INS integration, the larger gross errors can be easily detected by using the IGG III weight function. However, small ranging errors could appear when the signal occlusion is not so serious and conventional method may not be effective in this case. For the proposed WGINS, the obstructed satellites can be selected out and down-weighted, that is, the impacts of small ranging errors can also be mitigated. As the proposed algorithm does not conflict with conventional robust estimation, a better positioning performance can be achieved by combining the two methods.

In review of the proposed algorithm, there are two points that need to be emphasized. First, erroneous judgement is unavoidable, because the occlusion model is not so accurate. Second, as the shadowing effect on pseudorange observations is difficult to be quantified, an empirical model is used, which may not coincident with the actual situations. However, one of the main purposes of this paper is to highlight the impacts of GNSS body shadowing on pseudorange observations, and further investigations should be conducted to develop a more refined model.

5. Conclusion

In this paper, a wrist-worn and tightly-coupled GNSS/INS integrated system (i.e., WGINS) for pedestrian positioning is proposed, which takes GNSS body shadowing into account. The impacts of GNSS body shadowing on pseudorange observations are investigated quantitatively according to the tests conducted in an open-sky environment. Then, a specifically designed INS-based PDR algorithm is proposed, which can output high-frequency position and attitude information. Finally, utilizing the prior information, the obstructed satellites can be detected, and an empirical weight model is established to mitigate the impacts of GNSS body shadowing.

To evaluate the positioning performance of the proposed algorithm, three participants are involved in data collection. Both wrist-worn PDR and GNSS/INS integration algorithms have been tested. For PDR results, it is verified that the level-arm must be considered in wrist-worn mode. Horizontal position error of 4.88 m (RMS) has been achieved for the proposed INS-based PDR, with approximately 710 m of walking distance in 10 min. For GNSS/INS integration results, it is observed that the impacts of GNSS body shadowing cannot be ignored. Using the proposed weight model for the shadowed GNSS observations, the degradation can be effectively mitigated, and the horizontal position error is reduced from 2.42 m to 1.71 m (RMS).

For the future work, some issues should be further investigated. First, a more refined occlusion model should be established in future work. In addition, the experimental scope could be further expanded. For example, the performance of the proposed method could be evaluated when the pedestrian performs irregular actions such as waving or running. Moreover, the proposed algorithm is only tested in an open-sky environment, more tests in typical urban environments should be conducted.

CRediT authorship contribution statement

Xiaoji Niu: Writing – review & editing, Supervision, Conceptualization. **Zhihao Liu:** Writing – original draft, Validation, Software. **Jian Kuang:** Writing – review & editing, Methodology, Funding acquisition. **Longyang Ding:** Visualization, Project administration, Investigation.

Declaration of competing interest

The authors declare that they have no known competing financial interests or personal relationships that could have appeared to influence the work reported in this paper.

Acknowledgments

The authors thank Dazhou Xia and Shiyi Chen for supporting data collection and thank Hailiang Tang and Liqiang Wang for providing experimental facilities. This work was supported by Hubei Provincial Natural Science Foundation Program (No. 2023AFB021) and the Fundamental Research Funds for the Central Universities (No. 2042023kf0124).

Data availability

Data will be made available on request.

References

[1] L.E. Diez, A. Bahillo, J. Otegui, T. Otim, Suitability analysis of wrist-worn sensors for implementing pedestrian dead reckoning systems, IEEE Sensors J. 18 (12) (2018) 5098–5114.

[2] Y. Li, J. He, G. Huang, Z. Xie, Development status and trends of wearable smart devices on wrists, Cognit. Comput. – ICCC 2018 (10971) (2018) 119–129.

[3] X. Zhang, X. Tao, F. Zhu, X. Shi, F. Wang, Quality assessment of GNSS observations from an Android N smartphone and positioning performance analysis using time-differenced filtering approach, GPS Solut 22 (2018) 70.

[4] D. Weng, X. Gan, W. Chen, S. Ji, Y. Lu, A new DGNSS positioning infrastructure for Android smartphones, Sensors 20 (2) (2020) 487.

[5] X. Yan, C. Liu, M. Jiang, M. Yang, W. Feng, M. Zhong, L. Peng, Performance analysis of oceanographic research vessel precise point positioning based on BDS/GNSS RTK receivers, Measurement 211 (2023) 112637.

[6] L. Wang, P.D. Groves, M.K. Ziebart, Smartphone shadow matching for better cross-street GNSS positioning in urban environments, J. Navigation 68 (3) (2015) 411–433.

[7] D. Weng, W. Chen, M. Ding, S. Liu, J. Wang, Sidewalk matching: a smartphone-based GNSS positioning technique for pedestrians in urban canyons, Satell. Navig. 6 (4) (2025).

[8] M. Cheffena, Physical-statistical channel model for signal effect by moving human bodies, J Wireless Com Network 2012 (1) (2012) 77.

[9] K.A. Al Mallak, M. Nair, G. Hilton, T.H. Loh, M.A. Beach, Characterisation of human body shadowing in millimetre wave systems, in: 15th European Conference on Antennas and Propagation (EuCAP), 2021, pp. 1–5.

[10] L. Wu, S. Guo, L. Han, C. Anil Baris, Indoor positioning method for pedestrian dead reckoning based on multi-source sensors, Measurement 229 (2024) 114416.

[11] W. Kao, C. Chen, J. Lin, Step-length estimation using wrist-worn accelerometer and GPS, Proceedings of the ION GNSS+ 2011 (2011) 3274–3280.

[12] J. Qian, J. Ma, L. Xu, R. Ying, W. Yu, P. Liu, Investigating the use of MEMS based wrist-worn IMU for pedestrian navigation application, Proceedings of the ION GNSS+ 2013 (2013) 1057–1064.

[13] H.T. Duong, Y.S. Suh, Walking parameters estimation based on a wrist-mounted inertial sensor for a walker user, IEEE Sensors J. 17 (7) (2017) 2100–2108.

[14] L.E. Diez, A. Bahillo, A.D. Masegosa, A. Perallos, L. Azpilicueta, F. Falcone, J. J. Astrain, J. Villadangos, Signal processing requirements for step detection using wrist-worn IMU, in: International Conference on Electromagnetics in Advanced Applications (ICEAA), 2015, pp. 1032–1035.

[15] Y. Cho, H. Cho, C.M. Kyung, Accurate and robust walking speed estimation with adaptive regression models for wrist-worn devices, IEEE Sensors J. 20 (18) (2020) 10744–10755.

[16] S. Chandrasekaran, M. Lueken, S. Leonhardt, U. Gandhi, T. Laurentius, C. Bollheimer, C. Ngo, Step length estimation with wearable wrist sensor using ANN, in: 44th Annual International Conference of the IEEE Engineering in Medicine & Biology Society (EMBC), 2022, pp. 1125–1128.

[17] C. Jiang, Y. Chen, C. Chen, J. Jia, H. Sun, T. Wang, J. Hyyppa, Implementation and performance analysis of the PDR/GNSS integration on a smartphone, GPS Solut 26 (3) (2022) 81.

[18] T. Takasu, A. Yasuda, Development of the low-cost RTK-GPS receiver with an open source program package RTKLIB. The International Symposium on GPS/GNSS, 2009.

[19] X. Zhang, M. Wu, W. Liu, X. Li, S. Yu, C. Lu, J. Wickert, Initial assessment of the COMPASS/BeiDou-3: new-generation navigation signals, J. Geod. 91 (10) (2017) 1225–1240.

[20] S.J. Ambroziak, L.M. Correia, R.J. Katulski, M. Mackowiak, C. Oliveira, J. Sadowski, K. Turbic, An off-body channel model for body area networks in indoor environments, IEEE Trans. Antennas Propagat. 64 (9) (2016) 4022–4035.

[21] J. Kuang, X. Niu, X. Chen, Robust pedestrian dead reckoning based on MEMS-IMU for smartphones, Sensors 18 (5) (2018) 1391.

[22] R. Chen, L. Pei, Y. Chen, A smart phone based PDR solution for indoor navigation, Proceedings of the ION GNSS+ 2011 (2011) 1404–1408.

[23] K. Kunze, P. Lukowicz, K. Partridge, B. Begole, Which way am I facing: inferring horizontal device orientation from an accelerometer signal, Int. Symposium Wearable Comput. (2009) 149–150.

[24] L. Wang, Z. Li, N. Wang, Z. Wang, Real-time GNSS precise point positioning for low-cost smart devices, GPS Solut 25 (2) (2021) 69.

[25] Y. Yang, H. He, G. Xu, Adaptively robust filtering for kinematic geodetic positioning, J. Geod. 75 (2001) 109–116.

[26] Y. Li, J. Mi, Y. Xu, B. Li, D. Jiang, W. Liu, A robust adaptive filtering algorithm for GNSS single-frequency RTK of smartphone, Remote Sens. (Basel) 14 (24) (2022) 6388.